

A Wind Tunnel Rig to Study the External Fan Cowl Separation Experienced by Compact Nacelles in Windmilling Scenarios

Kshitij Sabnis* and Holger Babinsky†

Department of Engineering, University of Cambridge, Cambridge, CB2 1PZ, UK

Luca Boscagli‡, Avery Swarthout§, Fernando Tejero¶ and David MacManus||

Centre for Propulsion Engineering, Cranfield University, Cranfield, MK43 0AL, UK

Christopher Sheaf**

Installation Aerodynamics, Rolls-Royce plc, Derby, DE24 8BJ, UK

Ultra high-bypass ratio aircraft engines adopt slim fan cowl profiles which are sensitive to separation on their external surfaces under diversion windmilling conditions, when engine shutdown occurs during cruise. A two-dimensional wind tunnel rig is developed to investigate the separation mechanisms experienced by aero-engine nacelles in such scenarios to establish the detailed aerodynamics. The tunnel flow field with entry Mach number 0.65 broadly replicates the expected diversion windmilling flow behaviour for a full-scale nacelle, featuring a supersonic region which terminates in a normal shock wave on the external fan cowl surface. For the three conditions investigated, which relate to different engine mass-flow rates, the response of the boundary layer in this region progresses from remaining fully attached through to well-established separation. However, the rig Reynolds number based on nacelle lip thickness is about 1.2×10^6 , roughly one-third of full scale, resulting in a transitional rather than turbulent shock-boundary-layer interaction. Nevertheless, simple simulations correctly predict the wind tunnel flow field, except for the precise boundary-layer response to normal shock waves, and so experimental data from the rig can be used to validate relevant computational methods.

I. Introduction

THERE is a pressing need to allow for sustainable growth of the civil aviation industry by reducing the environmental impact of commercial aircraft. This requirement has led to the European Commission setting the aviation sector challenging targets under the FlightPath 2050 vision, namely to reduce fuel consumption by 75% and perceived noise by 65% before 2050 [1]. A promising way to achieve these goals with current technology involves improving the propulsive efficiency of aircraft engines by increasing the engine bypass ratio. In particular, ultra high-bypass ratio (UHBR) engines allow considerable performance improvements towards achieving the required fuel burn reductions [2]. These UHBR engines require significantly larger fans, which require the engine nacelles to also be increased in cross-section. However, if the nacelles were also proportionally longer there would be a corresponding increase in drag. To avoid this detrimental effect, novel UHBR nacelles need to be more compact by minimising both thickness and length while satisfying aerodynamic design requirements [2, 3].

Nacelle design is typically optimised for cruise operating conditions [4]. In certain off-design scenarios, however, the compact nature of UHBR nacelles can result in flow fields which exhibit substantial deviations from the baseline case. One flight regime which is expected to be potentially problematic is at engine shutdown during the cruise phase of flight, termed “diversion windmilling”. In windmilling scenarios such as this, the low mass-flow rate captured by the engine causes the stagnation point to move further inside the nacelle lip (Fig. 1). Since the compact nacelle geometries

*Research Associate, Department of Engineering, University of Cambridge.

†Professor of Aerodynamics, Department of Engineering, University of Cambridge, AIAA Fellow.

‡Research Fellow, Centre for Propulsion Engineering, Cranfield University.

§PhD Student, Centre for Propulsion Engineering, Cranfield University.

¶Lecturer in Propulsion Systems Design, Centre for Propulsion Engineering, Cranfield University.

|| Professor of Propulsion Aerodynamics, Centre for Propulsion Engineering, Cranfield University.

**Installation Aerodynamics Specialist, Installation Aerodynamics, Rolls-Royce plc.

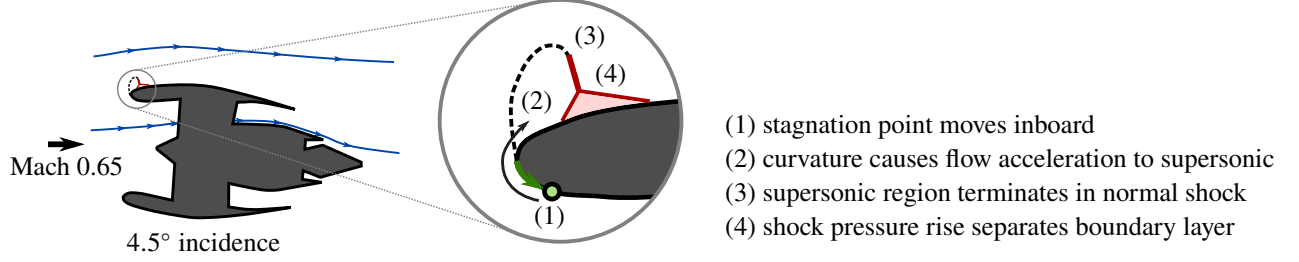


Fig. 1 Schematic of the flow separation mechanism for diversion windmilling.

Table 1 Operating conditions for the on-design cruise phase and the off-design windmilling scenarios.

case	height (m)	MFCR	FNPR	M_∞	α (deg)
cruise	10,700	MFCR _{cru}	FNPR _{cru}	0.85	4.5
diversion windmilling	6100	MFCR _{div}	1.32	0.65	4.5

necessarily have a more aggressive curvature at the leading edge, the inboard movement of the stagnation point results in substantial acceleration of the flow as it follows the highly-curved lip geometry. With a Mach 0.65 inflow, the flow acceleration around the nacelle lip creates a supersonic region. The normal shock which terminates this region can separate the boundary layer on the external nacelle surface [5].

Any significant detachment of the boundary layer around the upper external surface of the fan cowl during engine shutdown is problematic. In a situation where thrust is already reduced, this separation increases the drag and could result in adverse interactions with the wing flow field, which is especially relevant for configurations where the engine is installed close to the wing [5]. As a result, external fan cowl separation results in a considerable, negative impact on aircraft performance. Nevertheless, the precise separation behaviour remain poorly understood due to the complex underlying fluid mechanics, with the external fan cowl boundary layer subjected to strong favourable and adverse pressure gradients in close succession. Furthermore, due to these complexities, the flow field is not reliably computed by the Reynolds-averaged Navier–Stokes (RANS) methods typically used in industry, which is particularly problematic for nacelle designers [6, 7]. These difficulties are compounded by a notable lack of high-quality experimental reference data which can be used to validate relevant numerical methods.

In order to address this lack of in-depth knowledge about the detailed aerodynamic behaviour, a quasi-two-dimensional transonic wind tunnel setup was recently developed to replicate the key flow physics underlying external fan cowl separation in diversion windmilling conditions [8]. The current study aims to assess the extent to which this rig reproduces the real flow problem, as required to investigate the detailed flow physics and provide validation data for improving the predictive capabilities of relevant computational methods.

II. Design of Wind Tunnel Rig

Rig development process using CFD

The underlying objective when designing the rig geometry for studying diversion windmilling is to ensure that the wind tunnel flow replicates the key flow physics experienced by a full-scale, installed nacelle. Figure 2 shows that, broadly speaking, this can be achieved by defining floor and ceiling liner contours using bounding streamlines extracted from a vertical plane through 3D computations of a full-scale nacelle. In practice, however, a more careful approach is adopted to ensure that the installed wind tunnel set-up does indeed reproduce the desired separation mechanisms. In order to achieve this, the rig development process, detailed in reference [8], is performed in three separate stages:

- **Stage 1: Selecting a representative nacelle geometry** An optimisation procedure is conducted to determine a nacelle geometry for a full-scale installed UHBR engine that provides the best aerodynamic performance at cruise whilst satisfying constraints to ensure that the adverse effects in off-design situations are not too severe.
- **Stage 2: Analysis of flow field for full-scale nacelle** Preliminary 3D RANS computations are performed on a

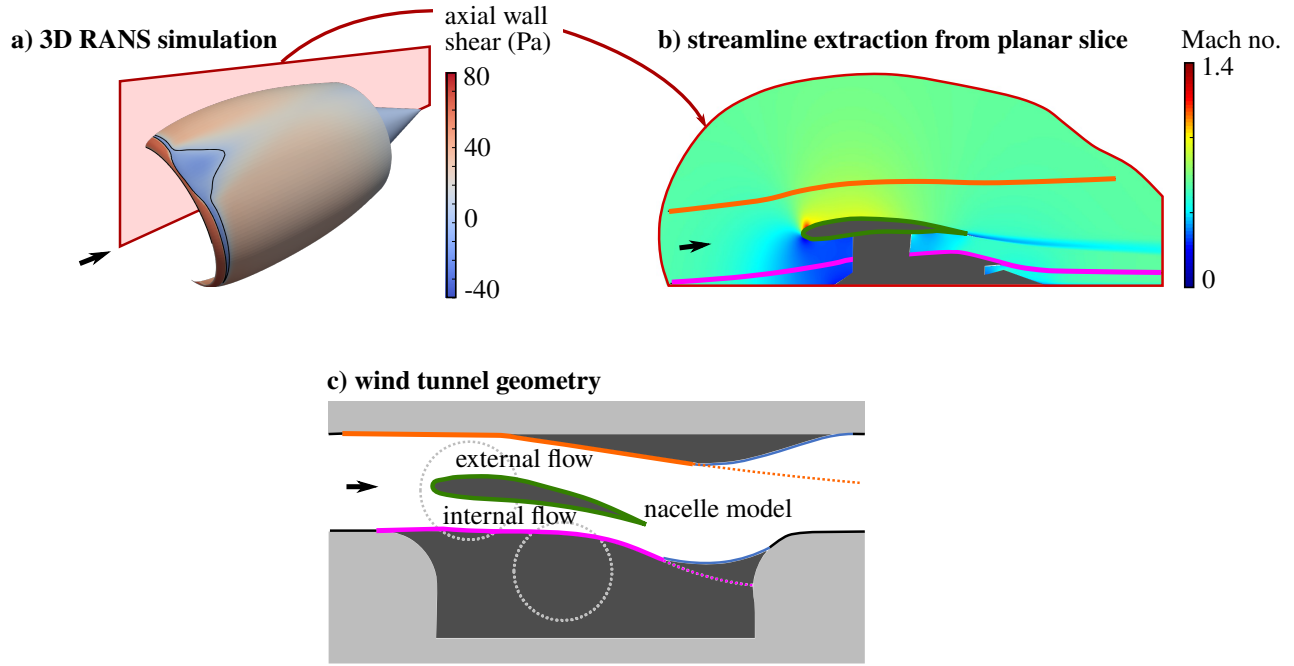


Fig. 2 Schematic generation of the rig geometry for diversion windmilling: a) 3D RANS simulations of the entire nacelle; b) streamlines from a slice through the vertical plane; c) the wind tunnel geometry with wall contours defined by extracted streamlines.

full-scale, three-dimensional nacelle for the diversion windmilling scenario, with relevant parameters perturbed about their nominal values to better understand their effects on the flow field.

- **Stage 3: Detailed rig design** The size of the nacelle model, its interface with the existing wind tunnel structure and the mechanism of mass-flow split control are determined using 2D RANS computations of the test rig as well as 3D RANS computations which account for the wind tunnel sidewalls.

Stages 1 and 2 of the rig development process require RANS computations of the full-scale nacelle whilst Stage 3 simulates the wind tunnel flow path. These computations may not capture all the flow physics entirely accurately but they are still thought to be instructive in guiding the design of the wind tunnel rig. All computations are conducted over a multi-block, fully-structured mesh with near-wall resolution, $y^+ \approx 1$. A double-precision density-based solver with an implicit time-integration formulation is used to solve the compressible, steady Favre-averaged Navier–Stokes equations. The computation of the numerical fluxes is based on a Roe scheme with the Green–Gauss method for spatial discretisation. Viscosity is calculated using Sutherland’s law [9] and, with the exception of a small number of computations which specifically investigate boundary-layer transition, the computations are run as fully turbulent using the $k-\omega$ shear-stress transport turbulence model [10].

Stage 1: Selecting a Representative Nacelle Geometry

The representative 3D non-axisymmetric baseline nacelle is designed for a long-range aircraft at $M_\infty = 0.85$ with a compact, dual separate jet exhaust. The nacelle design is left–right symmetric and there are four degrees of freedom applied to each of five control aerolines at 45-degree intervals from top to bottom (Fig. 3a). Appropriate values for these key nacelle dimensions are determined with a fully parametric definition that uses the intuitive class-shape transformation (iCST) method [13, 14]. The design process is based on a multi-point, multi-objective optimisation routine based on a well-established CFD methodology [4, 15–17].

The domain, shown in Fig. 3b, extends to a nominal far-field boundary at a distance of 40 engine-diameters from the nacelle. At this boundary, pressure far-field boundary conditions are used to impose: the scenario-dependent Mach number; the static pressure and temperature from the international standard atmosphere [18]; and the scenario-dependent altitude. The surfaces on the spinner, the intake, the fan cowl, the bypass duct and the core duct are all modelled as

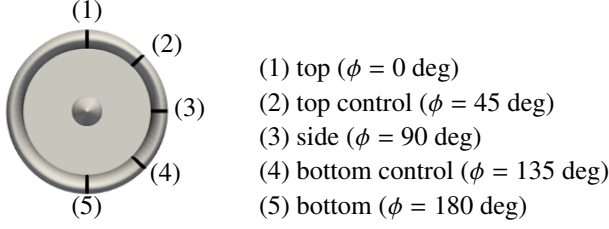
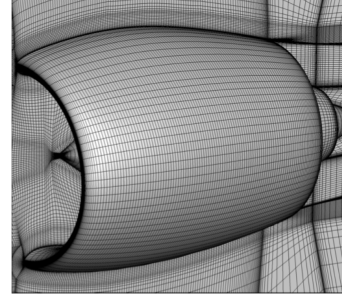
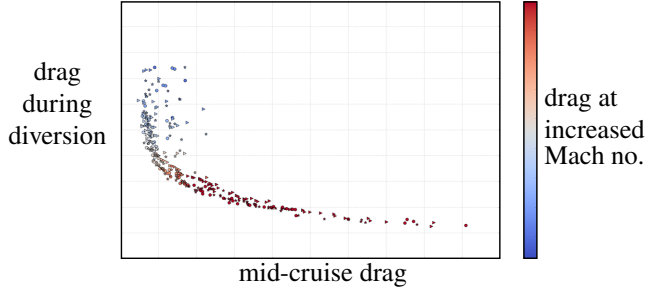
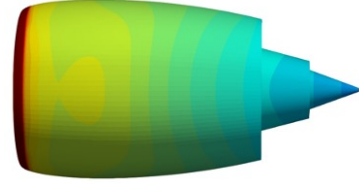
a) control aerolines**b) computational mesh****c) Pareto front****d) representative nacelle geometry**

Fig. 3 Generation of a representative nacelle geometry: a) control aerolines; b) mesh for 3D computations of full-scale nacelle; c) Pareto front; and d) representative geometry. The azimuthal coordinate, ϕ , goes from 0° at the upper lip to 180° on the lower lip. Adapted from Swarthout [11] and Tejero [12].

no-slip adiabatic walls. A target mass-flow pressure outlet boundary condition, calculated from the scenario-dependent mass-flow capture ratio value (Table 1), is prescribed at the fan face. Pressure-inlet boundary conditions are imposed at the inlets to the bypass duct and core duct with calculated total pressure and temperature values. A grid sensitivity was carried out for a representative mid-cruise condition. The grid-convergence index [19] was calculated to be 2.5% when three different meshes with 5×10^5 , 1×10^6 and 2×10^6 cells were considered, which is indicative of sufficient mesh independence for geometry optimisation.

Each nacelle is assessed using 3D computations of the full-scale geometry at six operating conditions, including the design cruise condition and diversion windmilling [20]. The initial Latin hypercube sampling (LHS) design space exploration uses 400 candidate geometries. The subsequent optimisation procedures evaluate 7450 different nacelle geometries, from which the Pareto front in Fig. 3c is constructed. The nacelle designs are then down-selected to minimise cruise drag whilst requiring that the length of any separation be less than 5% of the nacelle length, L_{nac} , resulting in the representative nacelle geometry presented in Fig. 3d. The mesh independence and validation of this numerical approach have been reported in a number of previous studies [4, 16, 21], and details of the methodology used for the current optimisation process are set out extensively by Swarthout [11].

Stage 2: Analysis of flow field for full-scale nacelle

There are five key parameters which are expected to govern the flow behaviour during diversion windmilling: the incidence angle (α), the incoming freestream Mach number (M_∞), the altitude, the mass flow capture ratio (MFCR, i.e. the ratio of the upstream streamtube capture area to the nacelle highlight area) and the fan nozzle pressure ratio (FNPR, i.e. the ratio of the total pressure at the nozzle inlet for the bypass stream to ambient static pressure). The altitude influences the local Reynolds number of the flow while the combined effect of α , FNPR and MFCR determines the stagnation point on the nacelle. Representative values for these parameters are listed in Table 1. For the conditions relevant to diversion windmilling, the Reynolds number based on lip thickness, Re_l , is estimated to be around 3.7×10^6 .

The flow field during diversion windmilling is analysed by considering the distribution of the isentropic Mach number, i.e. the Mach number defined by the local surface pressure, on the external fan cowl surface [11]. Figure 4 presents this quantity extracted from computations of the three-dimensional full-scale nacelle at the nominal diversion

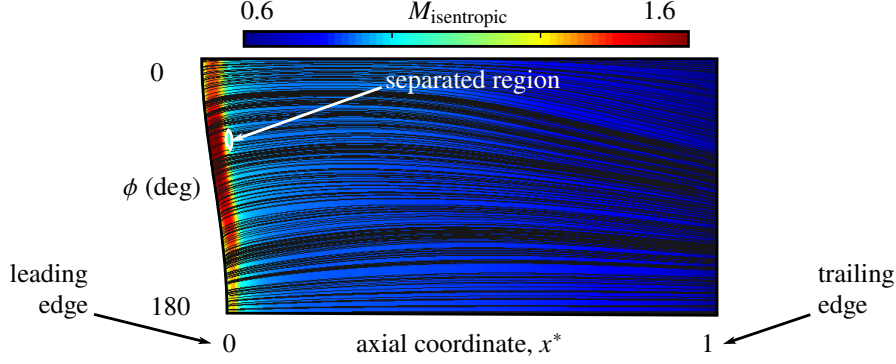


Fig. 4 Isentropic Mach number and surface streamlines for the nominal diversion windmilling conditions in Table 1. The non-dimensional streamwise coordinate, $x^* = x/L_{\text{nac}}$, goes from 0 at the leading edge to 1 at the trailing edge.

windmilling conditions (Table 1). This figure indicates that the flow over the nacelle forebody is transonic, with a supersonic region terminating in a normal shock. The pre-shock Mach number is roughly 1.5, resulting in a closed separation which is azimuthally positioned around $\phi = 45^\circ$. In the axial direction, this separated region covers less than 5% of the nacelle length.

When the incoming Mach number is increased to 0.7, Fig. 5a shows that the shock moves downstream and increases in strength. As a result, the separation length increases slightly, although it remains shorter than 5% of the nacelle length. Meanwhile, reducing the freestream Mach number to 0.6 (Fig. 5b) causes the shock to move upstream such that it weakens, resulting in attached flow over the entire nacelle. The flow field is also evaluated for a case with MFCR reduced by 11% in Fig. 5c. The shock location remains roughly constant but the peak pre-shock Mach number increases. Due to this enhanced shock strength, the extent of the separation is increased to about 20% of the nacelle length. When the FNPR is varied from 1.15 to 1.35 (either side of the nominal value) in Figs. 5d and 5e, the flow over the fan cowl and the extent of the shock-induced separation remain roughly unchanged. Thus, the peak cowl Mach number (which varies between 1.4 and 1.6) and the shock strength both show a sensitivity to freestream Mach number and to MFCR but are insensitive to FNPR.

Wind tunnel facility

The experimental rig is integrated into a blow-down transonic wind tunnel at the University of Cambridge. The wind-tunnel assembly, which is schematically depicted in Fig. 6a, is fed from a high-pressure reservoir into the settling chamber. Here, the flow passes through a number of flow straighteners and turbulence grids, followed by an 18:1 contraction with a round-to-rectangular transition. The test section, which is 114 mm wide and 1200 mm long, consists of an underlying tunnel structure, marked in light gray in Fig. 6a, onto which custom-built liner blocks (dark gray) can be bolted. The sidewalls of the wind tunnel are formed by removeable doors containing two optical-access windows with 203 mm diameter, which are indicated in Fig. 6a. The stagnation pressure can be set up to a maximum of 200 kPa, which permits some control over the Reynolds number of the flow in the test section.

There is an airfoil located downstream of the test section, as labelled in Fig. 6a. The flow at this point is choked to form a “rear throat”, and the angle of the airfoil sets the effective choking area. The area ratio between this rear throat and the test-section inlet determines the entry Mach number. In the test section itself, the nacelle model and the contours of the tunnel liner blocks are based on a planar slice through 3D RANS simulations, as depicted schematically in Fig. 2. Note that the geometry in Fig. 6b has been inverted for easier interface with the existing tunnel structure and reduced curvature of the liner contours, thus preventing tunnel wall separation and unwanted supersonic regions. As a result, the upper-bounding contour is representative of a streamline that is captured within the engine whereas the lower-bounding streamline belongs to the region external to the nacelle.

The nacelle model splits the test section flow into two channels. In the upper channel, the ceiling contour is perturbed to form a “bump” (Fig. 6b) which can be interchanged with one of different height to accurately control the upper-channel area. By throttling the flow through the upper channel in this way, the mass flow split between the two channels can be set, thus replicating variation in mass flow rate through the engine. Note that the upper channel flow is not choked, but instead the mass flow split is controlled by making the subsonic flow respond to imposed changes in the channel area.

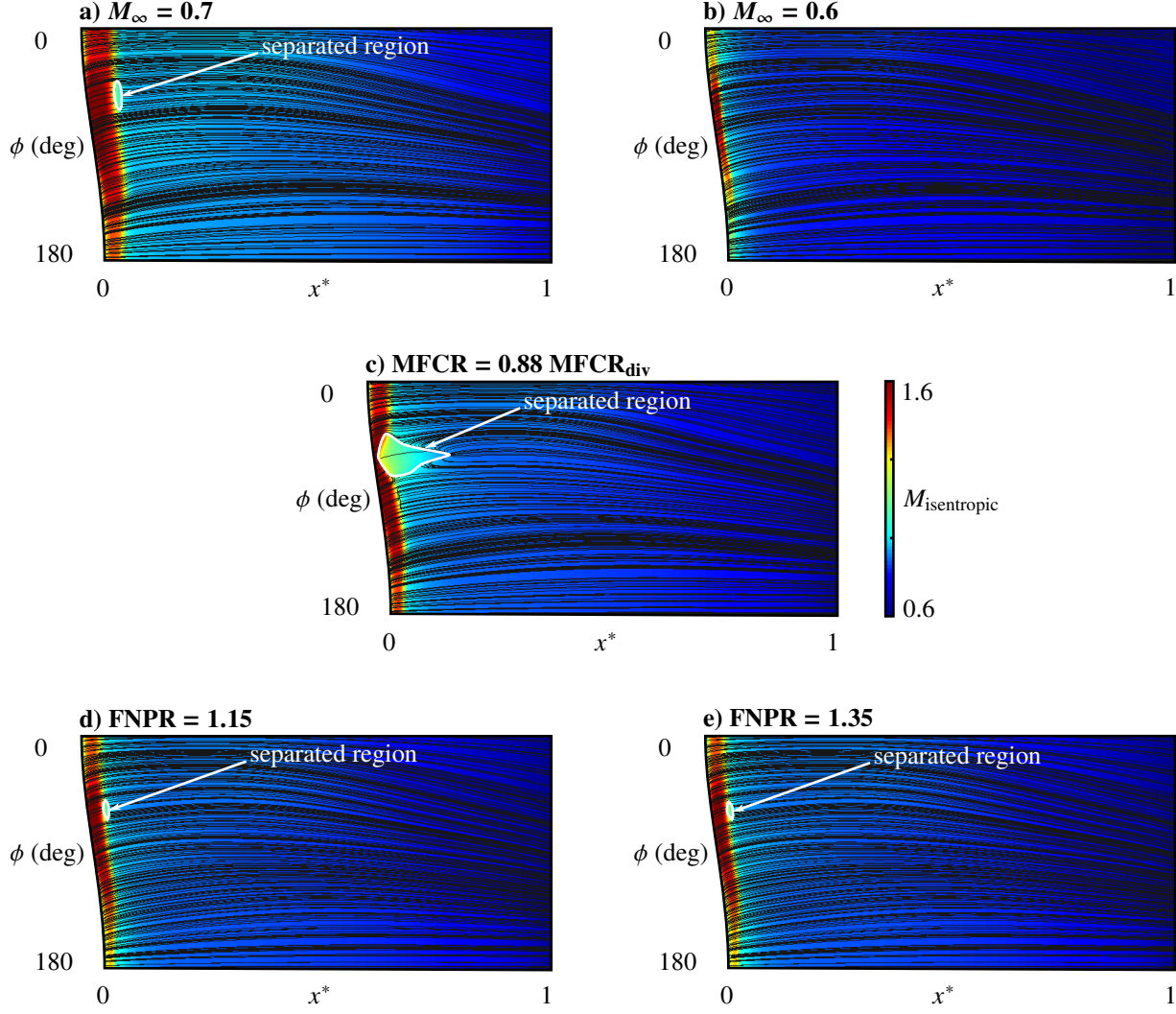


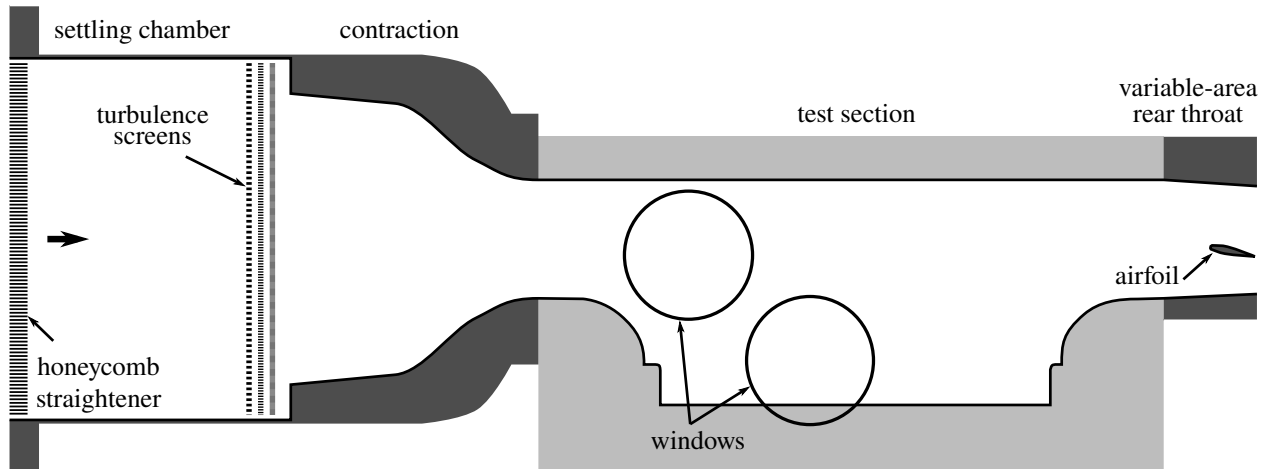
Fig. 5 Isentropic Mach number and surface streamline pattern for variations from the nominal diversion windmilling conditions in Table 1. Each plot perturbs one parameter from the nominal condition: a) increased Mach number; b) reduced Mach number; c) reduced MFCR; d) reduced FNPR; and e) increased FNPR.

Stage 3: Detailed rig design

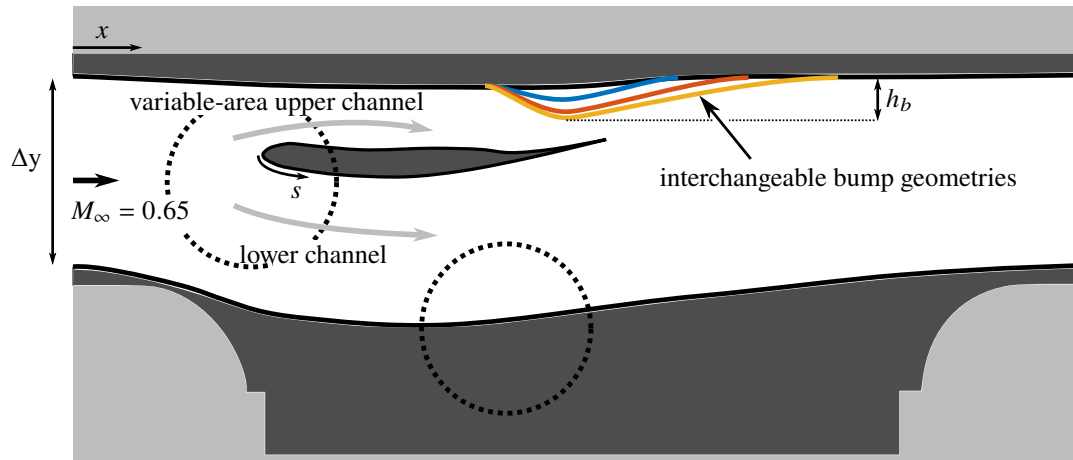
The detailed design of the rig uses 2D computations whose domain, presented in Fig. 7, encompasses the nacelle aeroline and the bounding streamlines which are all modelled as viscous, adiabatic walls. The bounding streamlines are axially extruded at the inlet and outlet by about twice the rig inlet height to improve numerical stability. Total pressure and static pressure boundary conditions are imposed at the domain inlet and outlet, respectively. At the outlet a target mass flow is prescribed to achieve the desired inlet Mach number. Preliminary computations capture the effect of the ceiling bumps by controlling the dynamic head loss through a porous region marked in Fig. 7. However, there is no porous region for the more detailed design, in which the computations use different meshes for each bump geometry under consideration (Fig. 6b). A mesh-independence study is performed with three levels of mesh refinement using 4.3×10^4 , 6.5×10^4 , and 1.1×10^5 nodes. The medium of these three meshes is considered to be sufficiently mesh independent with a grid-convergence index of 0.04% when applied to peak isentropic Mach number [8].

The nacelle model itself is based on the side aeroline from the representative nacelle model developed in Stage 1. Due to structural rig constraints, a 1/14th nacelle model is the largest scale which can feasibly be installed into the test section. Despite this being a pressurised facility, the Reynolds numbers for the scaled model is $Re_t \approx 1.2 \times 10^6$, roughly one-third of the full-scale value, and so cannot quite replicate a full-scale nacelle in flight. The local flow

a) wind tunnel infrastructure



b) test section set up



c) photograph of installed rig

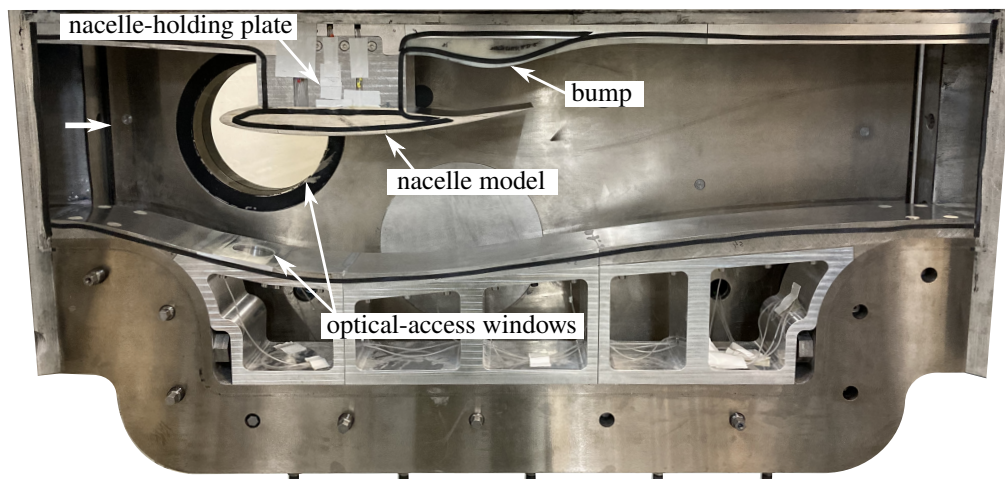


Fig. 6 a) Schematic of the wind tunnel facility into which the nacelle rig is integrated; b) detail of test section; c) photograph of installed rig.

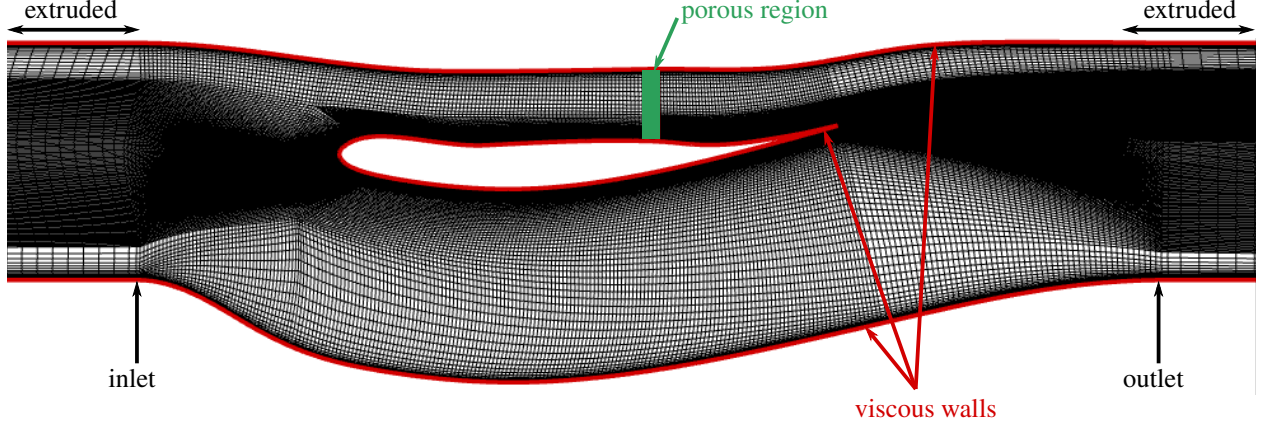


Fig. 7 Mesh for initial two-dimensional computations of the wind tunnel flow path. Later computations use the correct bump contour on the upper wall instead of the porous region to control mass-flow split.

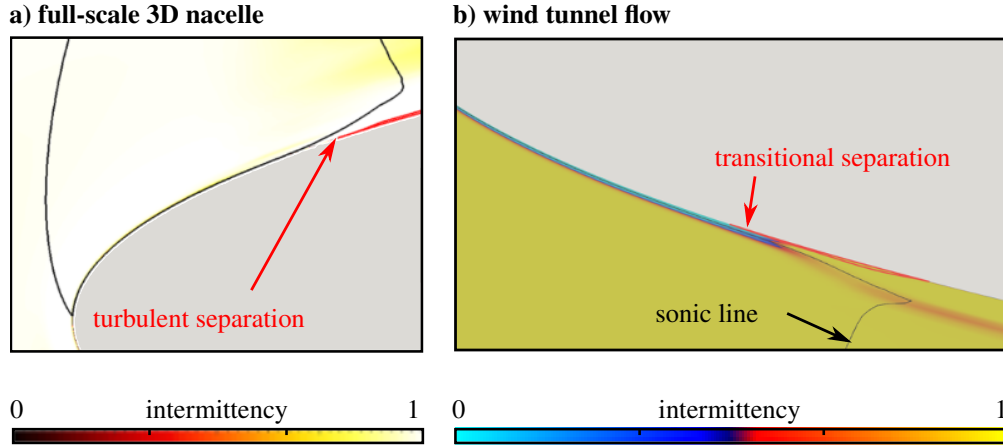


Fig. 8 Intermittency extracted from transitional boundary-layer computations of a) the three-dimensional nacelle at $Re_t = 3.7 \times 10^6$, and b) the wind tunnel flow path at $Re_t = 1.2 \times 10^6$. The intermittency takes values from 0 (laminar) to 1 (turbulent).

intermittency from full-nacelle computations using the $\gamma - Re_\theta$ boundary-layer transitional model (Fig. 8a) indicates that the boundary layer encountering the shock wave is turbulent. An analysis of transitional computations of the wind tunnel flow path with a 1/14th-scale nacelle model (Fig. 8b) indicates that the transition point for the boundary layer is very slightly downstream of the separation point, and thus the shock-boundary-layer interaction (SBLI) is likely to be transitional in nature. Since the model size and stagnation pressure are at their maximum limits, this discrepancy cannot be easily resolved. Instead, the nature of the incoming boundary layer needs to be monitored during physical wind tunnel experiments in order to assess whether transition needs to be encouraged through other means.

Another consideration relating to the size of the nacelle model is the effect of the tunnel ceiling and floor on the flow around the nacelle lip. If the nacelle model were too large, liner contours would be very close to the nacelle surface in relative terms. As a result, the tunnel walls would likely have a substantial effect on the flow around the nacelle lip. One way to check that these effects are not problematic for the geometry in Fig. 6b is to analyse whether the selected bounding streamlines in the full-scale nacelle computations are perturbed as the operating conditions are varied. Figure 9 shows that, even though the size of separation increases considerably in size as the MFCR is reduced by 11% (Figs. 4 and 5c), the contours of the selected bounding streamlines remain almost identical. Therefore, the geometry presented in Fig. 6b can be used to replicate changes in MFCR without the need to change wind tunnel liners.

The definitions of the ceiling and floor liner contours are based on streamlines extracted from the 3D nacelle computations (Fig. 2). However, in order to accurately reproduce the pressure distribution imposed on the nacelle, it is

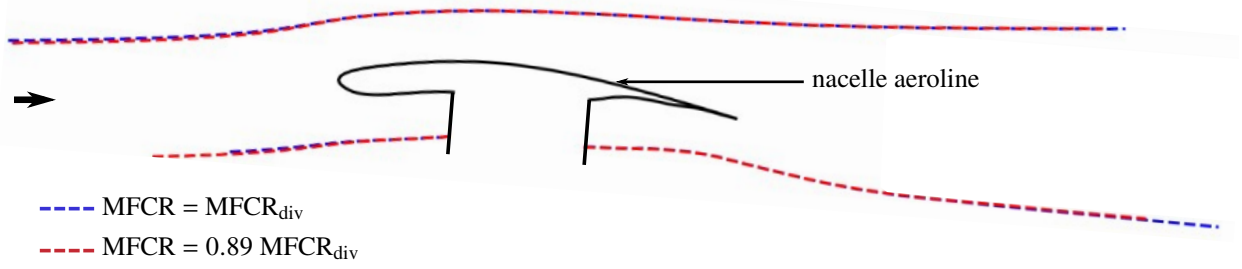


Fig. 9 Sensitivity of the bounding streamline shape on MFCR for diversion windmilling.

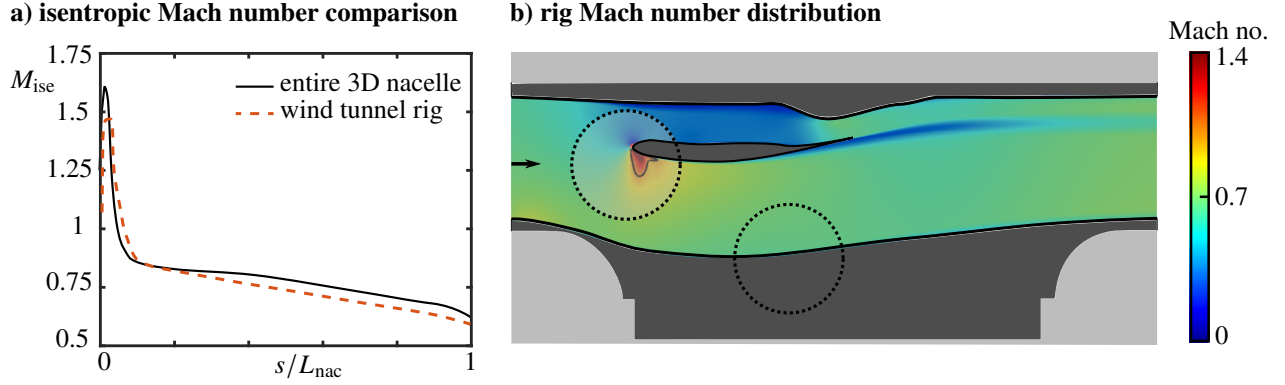


Fig. 10 a) Comparison between isentropic Mach number distribution on the external nacelle surface for the full-scale three-dimensional nacelle (with $MFCR = 0.88 MFCR_{div}$) and for the wind tunnel rig flow (with bump height normalised by tunnel height at entry, $h_b/\Delta y = 0.227$). b) Centreline Mach number distribution for the test rig geometry with $h_b/\Delta y = 0.227$.

necessary to account for the fact that a streamline divergence ratio of n in the vertical plane corresponds to an area variation of n^2 in the three-dimensional flow but of n for the two-dimensional wind tunnel. Therefore, the bounding streamlines are perturbed to correct the area ratios such that the Mach number variations from the 3D flow field are replicated. In order to achieve this, an initial Latin hypercube sampling (LHS) with 25 samples is used to adjust the lower bounding streamline, which follows a fully parametric description based on iCST [13]. As a result, the lower channel area distribution is modified in order to match the pressure distribution imposed on the rig nacelle model with the three-dimensional full-scale equivalent values (Fig. 10a).

Since the two-dimensional computations of the wind tunnel define no-slip boundary conditions on the floor and the ceiling, the boundary layers developing along these surfaces are already taken into account. However, such computations do not capture the boundary layers on the sidewalls which, as they develop, influence the effective flow area. In order to account for these sidewall boundary layers, the inverse design process is therefore performed using three-dimensional computations. These simulations are performed by extending the 2D mesh (Fig. 7) in the spanwise direction. 80 grid points are used in this direction across the tunnel span, with near-wall refinement close to the sidewalls to resolve the boundary layers in these regions. Viscous, adiabatic wall boundary conditions are applied to the sidewalls. Figure 10b presents an example of the test rig flow field for one of the designed bump contours. The Mach number distribution in the lower channel closely matches the target flow field, with a supersonic region around the nacelle lip terminating in a separated shock-boundary-layer interaction.

III. Experimental Techniques

A z-type schlieren system with a horizontal knife-edge enables visualisation of spanwise-averaged density gradients associated with flow features, such as boundary layers and shock waves. For each configuration, schlieren images are captured at 6400 frames per second using a Photron Fastcam Nova S6 camera, with an exposure time of 12.5 μs . The

infrared camera used to determine recovery temperature over the model is a liquid nitrogen-cooled FLIR SC7300 with an integration time of 160 μs and frame rate of 50 fps. For these measurements, the optical-access window is replaced with an equivalent window manufactured using multi-spectral grade zinc sulphide. In order to calculate surface temperatures, which are expected to be accurate to within ± 0.5 K, a paint emissivity of 94% and optical-path transmissivity of 97.6% are assumed, based on the calibration of an equivalent setup in the same facility.

Steady-state surface pressure measurements are conducted using about fifty 0.3 mm diameter static pressure taps connected to a differential pressure transducer (error: $\pm 1\%$) [22]. To determine surface pressure distributions using pressure-sensitive paint (PSP), the surface of interest is sprayed with a special polymer binder seeded with luminescent molecules. When irradiated by UV light, the resultant luminescence intensity ratio ($I_{\text{ref}}/I(p, T)$) is dependent on the local pressure, as specified by the Stern–Volmer relation [23]:

$$\frac{I_{\text{ref}}}{I(p, T)} = A(T) + B(T) \frac{p}{p_{\text{ref}}} \quad (1)$$

The luminescence is recorded using an Arducam 64MP camera, and the reference condition is taken with the wind tunnel off ($p_{\text{ref}} = 101$ kPa everywhere). The pressure in the separated flowfield varies from 50 – 200 kPa; this range of pressures is sufficiently large to provide reliable measurements [24]. In order to determine the values of $A(T)$ and $B(T)$ in the Stern–Volmer relation, in-situ calibration is performed using the static pressure taps. This calibration enables absolute pressure values on the target surface to be extracted from the measured light intensity. A comparison between static tap pressures and the calibrated PSP data places an error bound of 3% on these measurements. However, in regions where the thermal properties change (e.g. filler material or non-uniformities in the thermal conductivity of the underlying structure), the calibration is no longer valid and a much greater error is observed.

The topology of the separated flow field is surveyed using the time-averaged skin-friction lines from surface oil-flow visualisation. This technique involves coating the tunnel floor with a mixture made from paraffin, finely-powdered titanium dioxide, oleic acid and lubricating oil. This is an intrusive method and there is a small error due to oil-flow producing an inaccurate indication of separation location (by about 0.2 boundary-layer thicknesses = 0.6 mm) [25]. Nevertheless, oil-flow visualisation allows the flow topology to be determined, and comparisons of the size of separation regions between different setups are considered to be reliable.

The streamwise and vertical flow velocities, u and v respectively, are measured by two-component laser Doppler velocimetry (LDV). The flow is seeded with paraffin in the settling chamber; previous measurements of particle lag through a normal shock have placed the seeding droplet diameter in the range 200 – 500 nm [22]. The error in measured velocities due to the finite number density of seeding particles and due to the laser optics is 2% for u and 19% for v . In practice, LDV is not precisely a point-measurement technique, since velocities are averaged over a nominal ellipsoidal probe volume which spans 0.1 mm in the streamwise and vertical directions, and 2 mm in the spanwise direction. The positional accuracy of this probe volume is, approximately, $\Delta x \approx 0.2$ mm, $\Delta y \approx 0.005$ mm, and $\Delta z \approx 0.1$ mm.

Boundary-layer traverses are carried out with wall-normal resolution roughly 0.1 mm. The measured boundary-layer data is fitted to theoretical profiles. A Sun & Childs (1973) fit [26], adapted to include a van Driest compressibility correction, is used for the outer layer; this combines a log-law of the wall region with a Coles wake function. The viscous sublayer is modelled using a Musker (1979) fit [27]. These fitted profiles are then used to calculate characteristic boundary-layer integral parameters. This avoids errors caused by poor measurement resolution near the wall and therefore provides a more accurate estimate of integral boundary-layer parameters. The boundary-layer properties are determined in their incompressible forms, as these are less sensitive to variations in Mach number and require fewer assumptions to calculate from raw velocity data. The LDV data obtained in this study typically has around 15 measurement points within the boundary layer and the closest data point to the wall is at around $y^+ = 120$. This corresponds to an uncertainty in integral parameters of around 10% for an equilibrium turbulent boundary layer [28].

IV. Results & Discussion

In order to evaluate the extent to which the wind tunnel rig replicates the true diversion windmilling flow field, the entry Mach number is set to the nominal value, $M_\infty = 0.65$. Three bump heights are selected to cover the onset of boundary-layer separation, with preliminary RANS computations indicating that $h_b/\Delta y = 0.159$, 0.194 and 0.227 correspond to attached flow, incipient separation and fully-established separation, respectively. The data collected in the wind tunnel is used to answer two distinct questions:

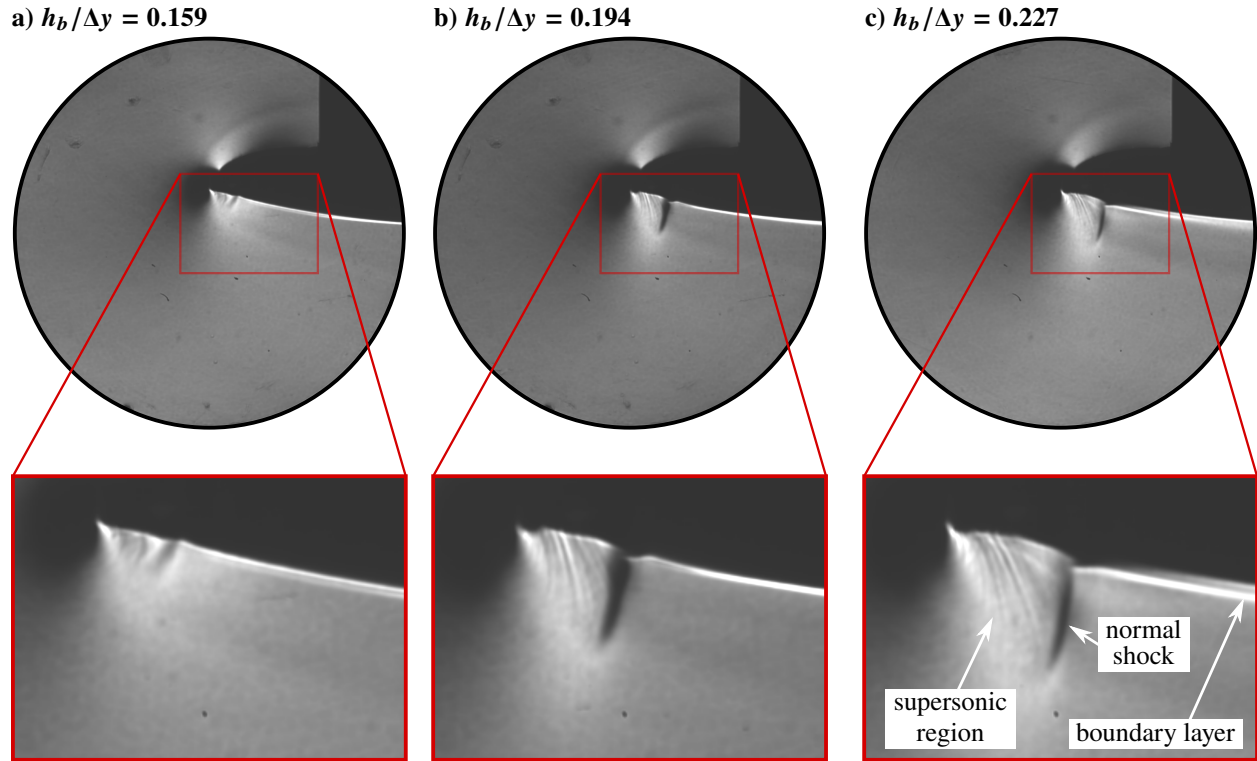


Fig. 11 Schlieren visualisation of wind tunnel flow for $h_b/\Delta y =$ a) 0.159, b) 0.194 and c) 0.227.

- **Is the flow field qualitatively as expected?**, i.e. does the flow field feature a supersonic region with a terminating normal shock and, over the range of mass flow splits studied, does the boundary layer go from attached to separated?
- **Is the flow field quantitatively as expected?**, i.e. does the experimental data match the preliminary RANS computations sufficiently well that the measurements can be used to develop relevant computational techniques?

Is the flow field qualitatively as expected?

Figure 11 presents schlieren visualisation of the diversion windmilling flow field for throttle valve bump heights, $h_b/\Delta y = 0.159, 0.194$ and 0.227 . In all three images, the dark region immediately upstream of the lip highlight is related to the optical distortion caused by the substantial density gradients in this region. The bright area below the nacelle model (i.e. on the external fan cowl surface of interest) is indicative of strong expansion, and the supersonic region can be visualised by the presence of weak waves emanating from the surface. The supersonic region is terminated by a normal shock, which appears in the schlieren images as a dark line approximately normal to the external fan cowl surface. The boundary layer downstream of the shock can be identified as a bright region which grows along the external nacelle surface. As the bump height is increased, representative of decreased mass flow through the engine, the supersonic region grows in size as the normal shock moves downstream. In addition, the structure of the shock–boundary-layer interaction progresses from a characteristic attached interaction with a smeared shock foot on Fig. 11a to a lambda-shock structure typical of a separated SBLI in Fig. 11c. A close examination of sequential frames of the instantaneous flow field for the intermediate case, $h_b/\Delta y = 0.194$, suggests that the boundary layer is incipiently separated.

The differences in flow field over nacelle's external surface are demonstrated by the surface pressure distribution depicted in Fig. 12. All three cases show a supersonic region terminating in a normal shock which is roughly uniform across the span of the tunnel. There is an apparent spanwise variation in measured pressure downstream of the shock–boundary-layer interaction. However, this feature is not physical but is instead an artefact of temperature variations caused by the thermally-conductive steel supports underneath the resin material near the tunnel sidewalls, which increase the local error in measured surface pressures in these regions. As the height of the bump increases and

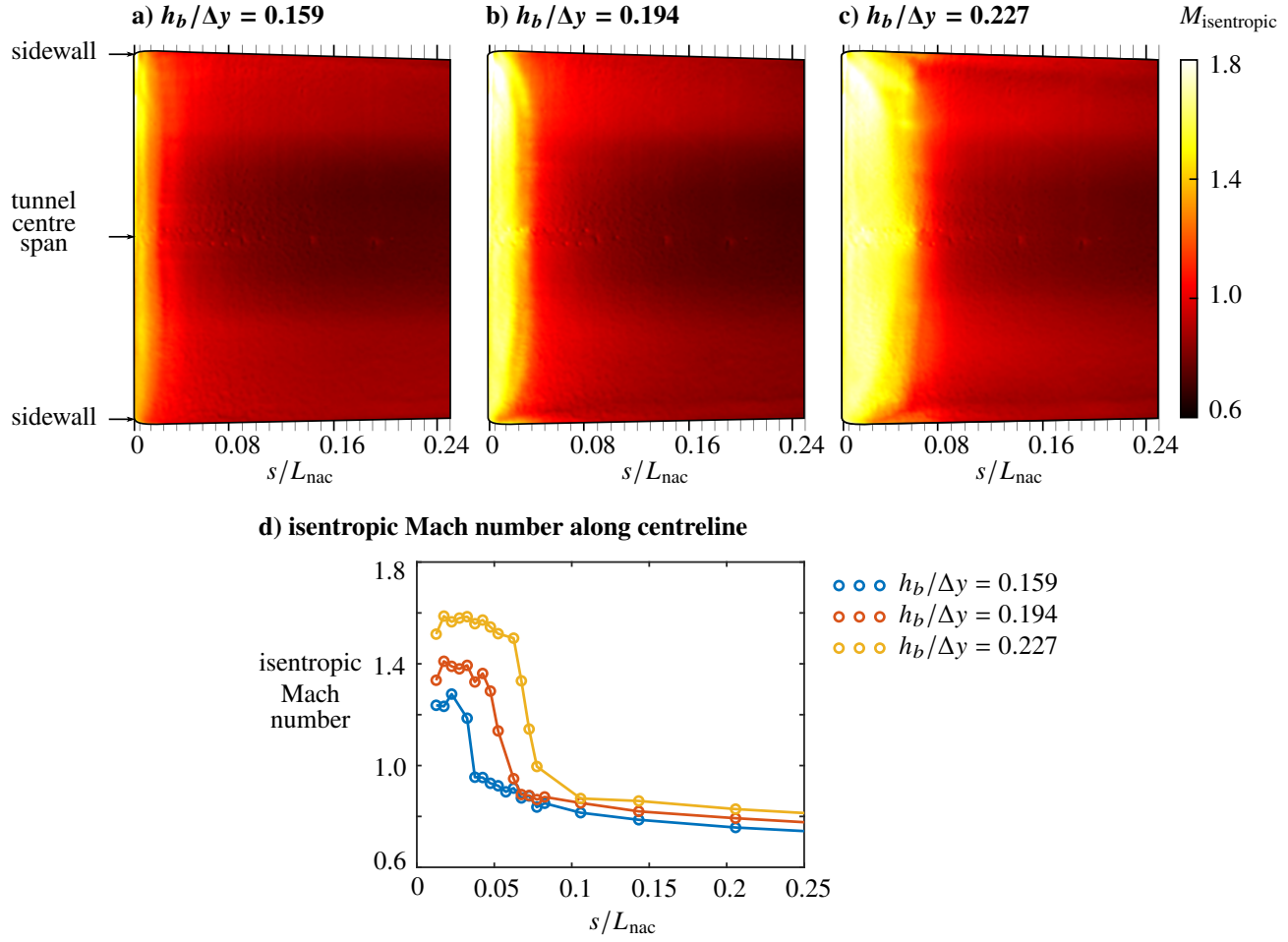


Fig. 12 Mach number distribution on the external nacelle surface obtained using pressure-sensitive paint for $h_b/\Delta y =$ a) 0.159, b) 0.194 and c) 0.227. d) Mach number distribution along the tunnel centreline.

the stagnation point moves inboard on the nacelle, Fig. 12d shows that the supersonic region becomes larger in size. In addition the Mach number immediately upstream of the shock increases, corresponding to a normal shock wave with greater strength.

The separation behaviour suggested by the schlieren images is also reflected in the oil-flow visualisation presented in Fig. 13. The position of the shock wave is evident in 13a from an accumulation of oil corresponding to a sudden reduction in shear stress. Nevertheless the streamlines everywhere (except for a small region near the corners) are in the streamwise direction, indicating that the boundary layer remains attached for this case. For a larger bump height, Fig. 13b reveals separation across much of the span of the tunnel which extends roughly $0.027 L_{nac}$ in the streamwise direction. In addition, noticeable corner separation has begun to develop near the tunnel sidewalls. Finally, at $h_b/\Delta y = 0.227$, there appears to be more substantial separation. The streamwise separation length on the tunnel centreline has increased to 4.4% of the nacelle length and the corner separation has also grown in extent.

The surface temperature distribution obtained from infrared thermography for $h_b/\Delta y = 0.227$ in Fig. 14 is affected by a number of factors: the starting temperature of the surface is the room temperature; the heat-transfer coefficient is affected by the boundary-layer state and the thermal conductivity of the underlying surface; and the equilibrium wind-on wall temperature is determined by the boundary-layer state, through the recovery factor, and the local free stream temperature, itself a function of stagnation temperature and local Mach number. Figure 14 shows that the regions towards each sidewall are cooler than in the central section. This is due to the underlying steel supports in these regions, which cools the surface faster than at the centre and also affects the PSP measurements in Fig. 12. Nevertheless, the behaviour of the central region of the flow in Fig. 14 is instructive as to the nature of the shock-boundary-layer interaction.

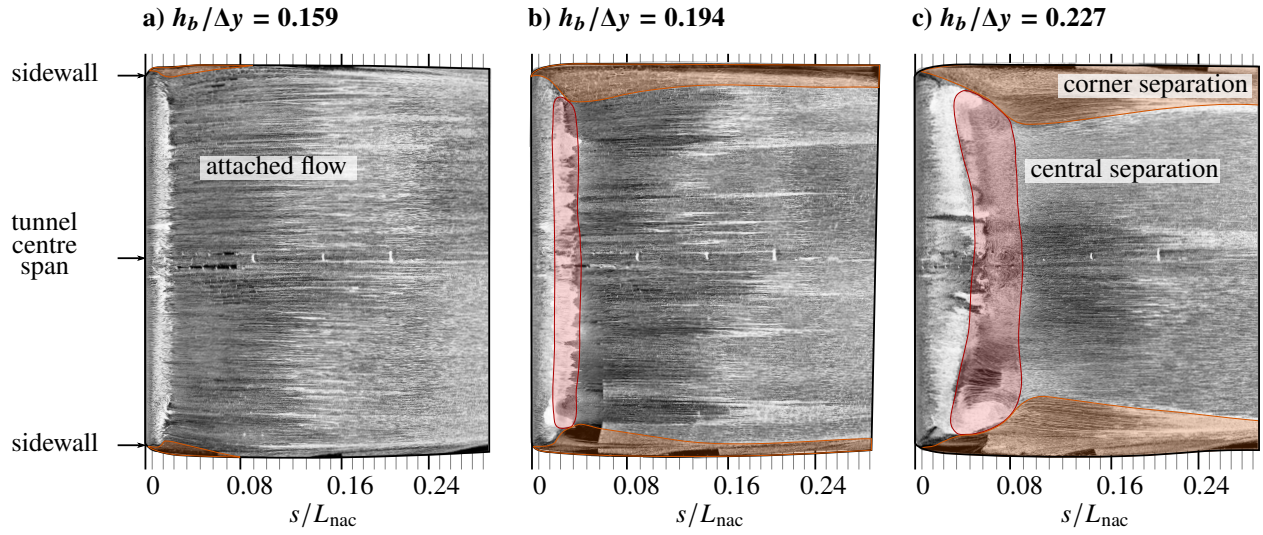


Fig. 13 Surface oil-flow visualisation on the external nacelle surface for $h_b/\Delta y =$ a) 0.159, b) 0.194 and c) 0.227. Regions of corner separation are highlighted in orange and the main central separation is marked in red.

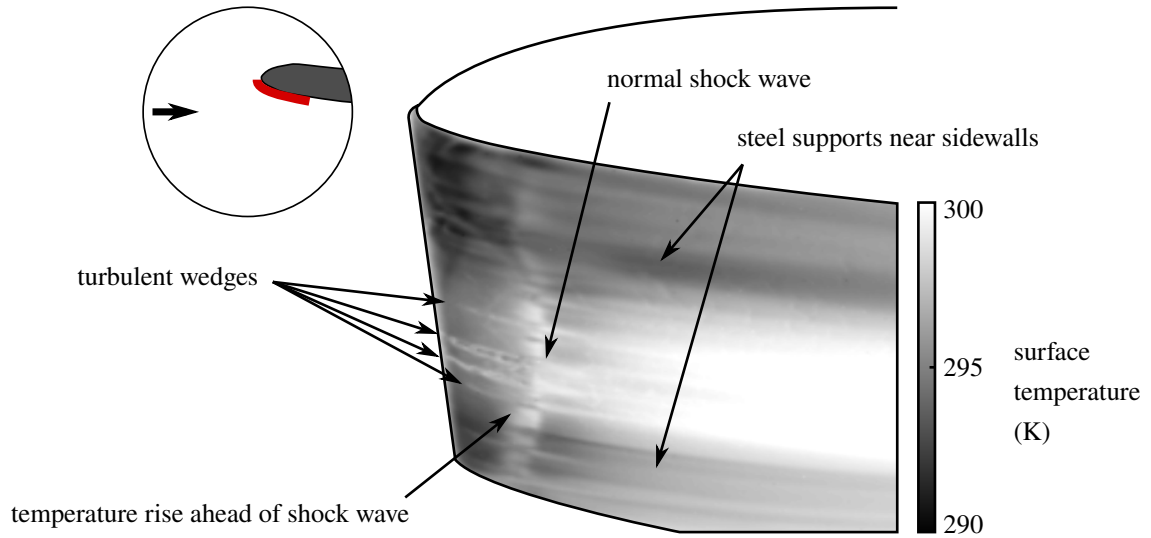


Fig. 14 Temperature distribution on the external fan cowl surface, determined using infrared thermography for $h_b/\Delta y = 0.194$.

The normal shock wave can be visualised in Fig. 14 as a sudden step change in temperature. Note that this appears to correspond to a decrease rather than increase in temperature immediately downstream of the shock wave, despite a reduction in Mach number, because the temperatures either side of the shock reach their equilibrium values at different rates. There are also a number of streamwise-running streaks with a higher temperature to the surrounding flow also visible in Fig. 14. These features correspond to a locally-increased recovery factor and so are believed to be turbulent wedges initiated at pressure taps or other small imperfections in the nacelle surface around the stagnation line. This suggests that the pre-shock boundary layer in the cooler regions surrounding the turbulent wedges is laminar or transitional in nature. Although there is insufficient information to conclusively distinguish between these two options, the significant number of turbulent wedges, the visible temperature increase ahead of the shock wave, and the angle of the leading lambda-shock wave in schlieren images in Fig. 11, suggests a transitional shock–boundary-layer interaction. Furthermore, the topology of the temperature distribution is consistent with a transitional interaction measured by Coschignano *et al.* for a similar flow field.

Is the flow field quantitatively as expected?

A quantitative assessment of the extent to which the wind tunnel rig replicates the expected flow field involves comparing wind tunnel data with the preliminary RANS computations used to design the rig. The geometry of these computations corresponds to the physical flow path in the test section (Fig. 6b), except that they do not capture the nacelle holding plates in Fig. 6c. In addition, the computations use nominal operating conditions for the rig rather than measured values. Nevertheless, a comparison of static pressure tap data and laser Doppler velocimetry measurements against equivalent values from these preliminary computations is believed to be instructive in evaluating whether or not the wind tunnel flow agrees with expectations.

Figure 15 presents a direct comparison of the static pressure data on the floor, ceiling and nacelle aeroline between experiment and CFD. The measured floor and ceiling pressure values in Figs. 15a and 15b, respectively, both show good agreement with the computational distributions with two notable exceptions. First, Fig. 15a shows that the lower wall Mach number distribution in computations for $h_b/\Delta y = 0.227$ is about 4% larger than the experimentally measured values. Secondly, the computations predict a noticeably lower Mach number than experiment in the upper wall region immediately ahead of the bump (Fig. 15b, which is caused by the preliminary computations not including the nacelle-holding plates). Apart from these two exceptions, the differences in isentropic Mach number are typically less than 1.1% on the lower wall and 2.2% on the upper wall, indicating good agreement between computation and experiment. Specifically for the purposes of replicating the design flow field, it is important that the pressure peak at the crest of the bump is reproduced accurately – in all three cases, Fig. 15c indicates that the measured position of this peak matches CFD to within 5 mm = $0.02\Delta y$ and the discrepancy in maximum Mach number is no larger than 0.02.

On the nacelle aeroline, Fig. 15d suggests that the static pressure taps located around the stagnation point of the nacelle, roughly on the tunnel centre span, broadly agree with computational data, with a typical deviation in Mach number of 0.02. Importantly, the location of stagnation point (i.e. the location where the isentropic Mach number reaches a minimum at zero) matches CFD to within the tap resolution, i.e. $0.001 L_{nac}$. In agreement with computations, the measured stagnation point moves by about 1.5 mm, or $0.004 L_{nac}$, around the internal surface of the nacelle, further from the lip highlight, as the bump height is increased. The isentropic Mach number distribution along the external surface of the nacelle also broadly agrees with CFD (Fig. 15e), with a downstream movement of the normal shock wave and increase in shock strength as the bump height increases. For all three bump heights, Fig. 15f shows that the measured isentropic Mach number lies within 4% of the computational values. Importantly, the shock wave position is consistent to within 0.9 mm ($\approx 0.002 L_{nac}$) and the pre-shock Mach number agrees with CFD to within 3%. However, the pressure rise through the normal shock wave is significantly more smeared in computations than experiment (Fig. 15f), which is the main contributor towards the quoted isentropic Mach number difference. Nevertheless, the overall pressure distribution on the nacelle model is thought to accurately represent the design values.

Another measure of the extent to which the wind tunnel flow matches expectations concerns the boundary-layer profile downstream of the shock–boundary-layer interaction. Figure 16 shows that, at $s/L_{nac} = 0.09$, the boundary layer becomes thicker and less full as the bump height increases, corresponding to a more severe shock–boundary-layer interaction. For the attached shock–boundary layer interaction with $h_b/\Delta y = 0.159$, Fig. 16a suggests that the entire velocity profile is captured accurately. The corresponding boundary-layer parameters listed in Table 2 quantify this agreement, with the freestream velocity, boundary-layer thickness, and displacement thickness correct to within 0.4%, 2% and 17%, respectively. The computed boundary-layer profile corresponding to incipient separation (Fig. 16b) correctly predicts the freestream velocity (difference: 0.7%) and the boundary-layer thickness (difference: 6%). However,

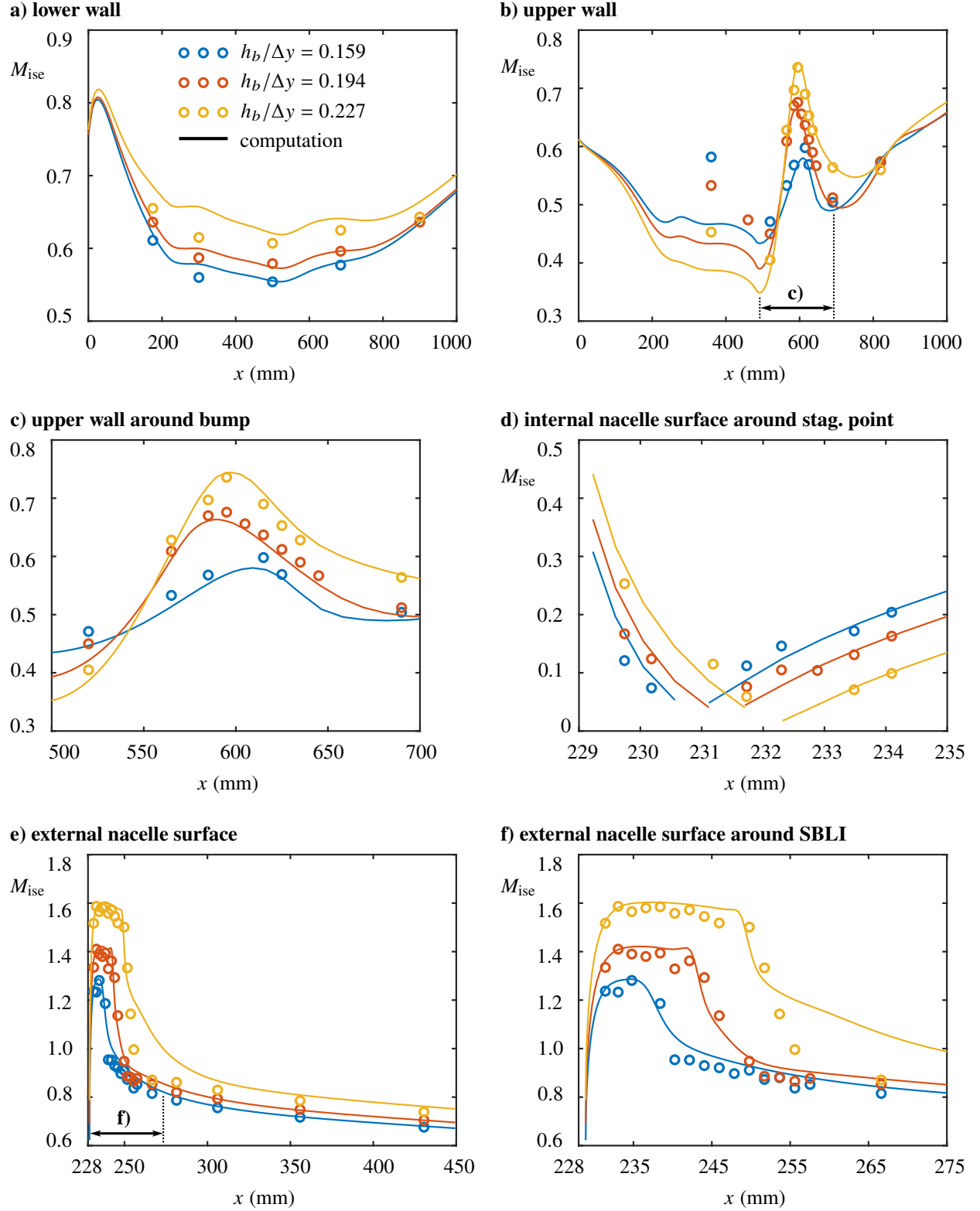


Fig. 15 Comparison between isentropic Mach number calculated from static pressure taps and extracted from computations on: a) the lower wall; b) the upper wall; c) the upper wall around the bump; d) the internal nacelle surface around the stagnation point; e) the external nacelle surface; and f) the external nacelle surface around the shock–boundary-layer interaction.

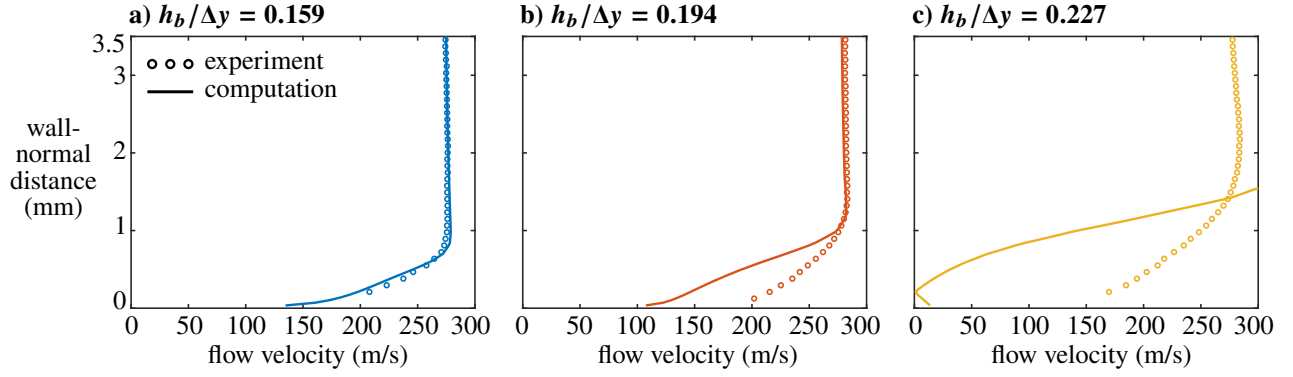


Fig. 16 Comparison between experimental and computational boundary-layer profiles downstream of the shock, at $s/L_{\text{nac}} = 0.09$ for $h_b/\Delta y =$ a) 0.159, b) 0.194 and c) 0.227.

Table 2 Integral boundary-layer parameters for velocity profiles at $s/L_{\text{nac}} = 0.09$, which are presented in Fig. 16.

normalised bump height, $h_b/\Delta y$		freestream velocity, u_∞ (m/s)	boundary-layer thickness, δ (mm)	displacement thickness, δ_i^* (mm)	momentum thickness, θ_i (mm)	shape factor H_i
0.159	experiment	276	0.86	0.134	0.094	1.42
	computation	277	0.84	0.157	0.105	1.50
0.194	experiment	282	1.29	0.162	0.120	1.35
	computation	280	1.21	0.316	0.182	1.74
0.227	experiment	281	1.71	0.317	0.215	1.48
	computation	335	2.46	0.860	0.392	2.19

the velocities within the boundary layer are significantly lower than in experiment, which causes the computational displacement thickness to be almost twice as large as the measured value. Figure 16c, for the most-separated case with $h_b/\Delta y = 0.227$, displays even more significant discrepancies, with poor prediction of the freestream velocity, boundary-layer thickness and boundary-layer shape. The differences in these quantities are listed in Table 2 to be 19%, 44% and 170%, respectively.

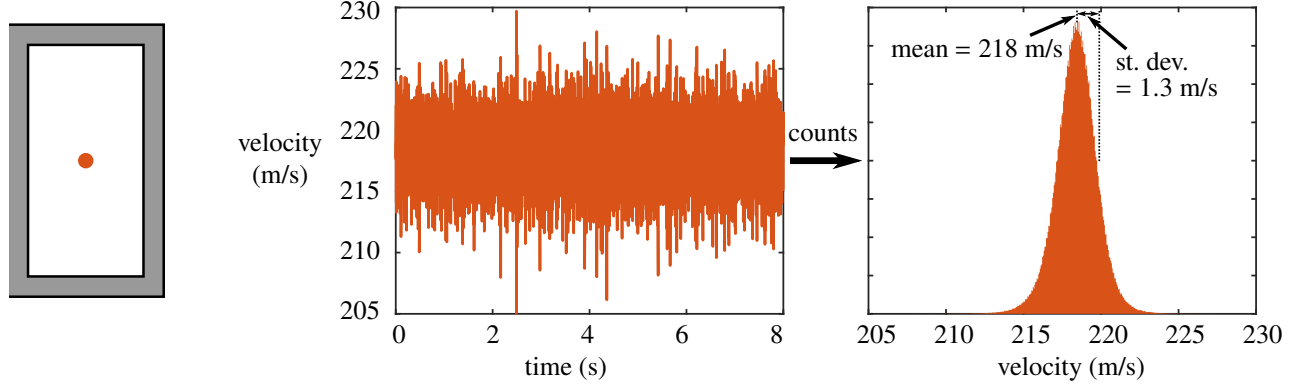
Discussion

The schlieren visualisation in Fig. 11 exhibits the expected diversion windmilling flow field, with a local supersonic region terminating in a normal shock wave. As the bump height increases, i.e. a lower mass flow through the engine, the stagnation point moves further inside the nacelle lip (Fig. 15d). As a result, there is greater flow acceleration around the lip and so the size of the supersonic region and the strength of the normal shock grows (Fig. 12). This causes boundary-layer separation to be initiated and then to grow (Fig. 13) which in turn causes the downstream boundary layer to be thicker and less healthy (Fig. 16) Therefore, the general mechanisms expected during diversion windmilling are exhibited in the wind tunnel rig.

However, infrared thermography suggests that the shock–boundary-layer interaction appears to be transitional (Fig. 14). This agrees with expectations from transitional RANS computations of the wind tunnel flow in Fig. 8b, however the full-scale nacelle is believed to exhibit a turbulent SBLI during diversion windmilling (Fig. 8a). The Reynolds number of the rig cannot be further increased through a larger model or higher stagnation pressure. It is therefore necessary to also measure the flow with an artificially-tripped flow, such as by increasing roughness around the nacelle lip, in order to assess how the current experiments extend to the full-scale scenario.

One possible way to assess the effect of transitional versus turbulent interactions uses the infrared image in Fig. 14, where there could be a different shock–boundary-layer interaction in the regions with the turbulent wedges compared to the laminar regions. However, the surface pressure distribution (Fig. 12) and the surface oil-flow pattern (Fig. 13) both suggest that the flow field is two dimensional except near the tunnel sidewalls, although it is worth noting that the latter

a) hot-wire anemometry



b) Pitot probe traverse on sidewall

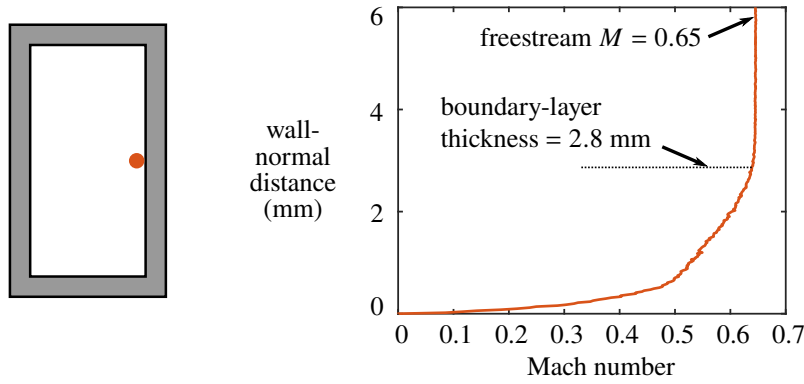


Fig. 17 Measurements collected in the entry plane for $h_b/\Delta y = 0.194$. a) Time-series and histogram of velocity data at centre of tunnel cross-section from hot-wire anemometry. b) Sidewall boundary-layer profile at the tunnel centre-height measured using a Pitot probe traverse.

technique is intrusive. A possible interpretation of the two-dimensional behaviour is that the shock–boundary-layer interaction behaves similarly in the laminar and turbulent regions. Further investigation of this hypothesis requires measurement of post-shock boundary-layer profiles not just on the tunnel centreline but across the entire span.

The preliminary RANS computations, originally used for rig design, appear to generally capture the floor and ceiling pressure distributions well for the three bump heights investigated, except in the region bounded by the nacelle-holding plates (Fig. 6c). On the nacelle model, the location of the stagnation line, the size of the supersonic region, and the Mach number of the normal shock all match experimental data (Fig. 15). In addition, the thickness of the boundary layer downstream of the SBLI is also well predicted (Fig. 16). However, with the exception of the case where the boundary layer remains attached through the SBLI, there is significant discrepancy in the velocity profile between experiment and CFD. This observation, along with the smearing of the normal shock pressure rise in computations, is one of the known limitations of RANS methods in predicting such flow fields targeted by the current study. The good agreement in other aspects of the flow field suggests that the experimental rig can provide valuable reference data to develop improved numerical techniques.

However, any such investigation requires the computations to match the physical wind tunnel flow path as closely as possible. This involves ensuring the precise installed geometry is used as the computational domain, such as including the nacelle-holding plates in the mesh. In addition, it is necessary to use measured operating conditions rather than nominal values. Finally, further information on the inlet boundary conditions is required, such as the freestream turbulence intensity and the incoming boundary-layer thickness on the tunnel walls. These inflow properties are therefore measured directly in the rig for $h_b/\Delta y = 0.194$. The turbulence intensity is measured to be 0.6% using hot-wire anemometry (Fig. 17a), whereas the boundary-layer thickness is assessed using a Pitot probe traverse at a representative location on the tunnel sidewall. The resulting boundary-layer profile, shown in Fig. 17b, therefore constitutes valuable

information to set up more representative computations of the test rig flow.

V. Conclusions

This paper presents a wind tunnel rig to investigate separation on the external surface of fan cowls for ultra-high bypass ratio engines in off-design scenarios. The prohibitive drag penalty when flow detachment occurs motivates the need to better understand its onset and underlying physical mechanisms. External boundary-layer separation is particularly relevant to UHBR nacelles, which tend to feature more aggressive curvature around the nacelle lip compared to traditional engine fan cowl geometries. Diversion windmilling conditions, experienced at engine shutdown during cruise, are reproduced in a quasi-two-dimensional wind tunnel rig which is designed using a series of RANS computations. The 1/14th-scale nacelle model in the rig uses an aeroline extracted from a representative, optimised geometry for UHBR engines. The upper wall of the wind tunnel is based on a streamline from computations which is internal to the engine. Meanwhile, the contour of the lower wall is defined using an inverse-design process to impose a pressure distribution on the nacelle model which corresponds to that experienced by a full-scale, three-dimensional, installed nacelle. The flow Reynolds number is controlled by varying the stagnation pressure at which the tunnel is operated, the incoming Mach number is set by adjusting the effective flow area in a choked region downstream of the test section, and variations in the mass flow rate through the engine are replicated using a set of interchangeable bumps with different heights on the ceiling which throttle the flow in the channel above the nacelle model.

The current study aims to provide valuable information for aircraft and engine manufacturers so that they can design nacelles for UHBR engines which will exhibit optimal aerodynamic performance even in off-design conditions. To evaluate the extent to which the wind tunnel rig can achieve this aim, the flow field is assessed using: the maximum Reynolds number achievable in the rig, $Re_t \approx 1.2 \times 10^6$, roughly one-third of the full-scale value; the nominal diversion windmilling entry Mach number, $M_\infty = 0.65$; and three engine mass-flow rate scenarios. These three scenarios correspond to attached flow, incipient separation, and well-established separation on the external fan cowl surface. The separation behaviour is evaluated using flow visualisation and quantitative methods in order to determine whether the rig can be used to investigate the physical mechanisms underlying external fan cowl separation during diversion windmilling and whether experimental data from the rig is suitable to develop relevant numerical techniques.

The test rig replicates the expected flow behaviour around a full-scale nacelle, featuring a supersonic region around the external fan cowl surface which terminates in a normal shock. For reduced mass flow rate through the engine is reduced, i.e. an increase in bump height, it is observed that the stagnation point moves further inside the nacelle lip, the size of the supersonic region grows, the normal shock wave becomes stronger, boundary-layer separation is initiated then grows in size, and the downstream boundary layer becomes thicker. This general behaviour matches the flow field thought to occur around a full-scale, installed nacelle. However, since the rig cannot quite replicate the full-scale Reynolds number, the measured shock-boundary-layer interaction is transitional in nature, whilst the real scenario features a turbulent interaction. Therefore, it is important to conduct further experiments with forced transition in order to understand how the rig measurements relate to a full-scale nacelle. By also collecting data at inflow Mach numbers either side of the nominal condition, future measurements will provide insight into the physical mechanisms governing external fan cowl separation.

The degree to which the wind tunnel flow can be used to validate computational methods is assessed by comparing measurements with the simple RANS simulations used to design the rig. These computations correctly predict the three studied flow field to exhibit attached flow, incipient separation and well-established separation, respectively, suggesting the simulations can determine the onset of separation relatively well. The measured static pressure distributions demonstrate good agreement, although there are certain minor differences on the tunnel ceiling and floor. Importantly, the pressure distribution on the nacelle is predicted well: the difference between measured and computational stagnation point positions is about 0.1% of the nacelle length; the position of the computed normal shock agrees with experiment to within 0.2% of the nacelle length; and the pre-shock Mach number matches rig data to within 3%. The post-shock boundary layer is also well predicted in the attached scenario, although there are increasing discrepancies in the velocity profile as the extent of boundary-layer separation increases. These observations suggest that the flow field is generally well predicted with RANS simulations but there are some differences in areas where such simple methods are known to struggle, such as the boundary-layer response to normal shocks at Mach 1.4 and stronger. Therefore, by comparing the wind tunnel flow against RANS and higher-fidelity computations conducted by the ODIN consortium partners, numerical techniques relevant to diversion windmilling will be validated and further developed.

Acknowledgements

This project has received funding from the Clean Sky 2 Joint Undertaking (JU) under grant agreement number 101007598. The JU receives support from the European Union's Horizon 2020 research and innovation programme and the Clean Sky 2 JU members other than the Union. The authors would like to thank D. Martin, A. Luckett and C. Costello for operating the blow-down wind tunnel. The authors are also grateful to N. Atkins and W. Davis for loan and assistance with the operation of the infrared thermography camera.

References

- [1] Commission, E., "FlightPath 2050: Europe's vision for aviation," Tech. Rep. EUR 098 EN, Publications Office of the European Union, 2011.
- [2] Hughes, C., "The promise and challenges of ultra high bypass ratio engine technology and integration," Tech. Rep. HQ-STI-11-012, National Aeronautics and Space Administration, 2011.
- [3] Magrini, A., Benini, E., Yao, H.-D., Postma, J., and Sheaf, C., "A review of installation effects of ultra-high bypass ratio engines," *Progress in Aerospace Sciences*, Vol. 119, 2020, p. 100680.
- [4] Robinson, M., MacManus, D., Christie, R., Sheaf, C., and Grech, N., "Nacelle design for ultra-high bypass ratio engines with CFD based optimisation," *Aerospace Science and Technology*, Vol. 113, 2021, p. 106191.
- [5] Hoelmer, W., Youngmans, J., and Raynal, J., "Effect of Reynolds number on upper cowl flow separation," *Journal of Aircraft*, Vol. 24, No. 3, 1987, pp. 161–169.
- [6] Kalsi, H., and Tucker, P., "Numerical modelling of shock wave boundary layer interactions in aero-engine intakes at incidence," *Proceedings of ASME Turbo Expo 2018 Turbomachinery Technical Conference and Exposition*, Vol. 50985, GT2018-75872, American Society of Mechanical Engineers, 2018.
- [7] Oriji, U., and Tucker, P., "Modular turbulence modeling applied to an engine intake," *Journal of Turbomachinery*, Vol. 136, No. 5, 2014, p. 051004.
- [8] Boscagli, L., Tejero, F., Swarthout, A., MacManus, D., Sabnis, K., Babinsky, H., and Sheaf, C., "Design of a quasi-2D rig configuration to assess nacelle aerodynamics under windmilling conditions," *AIAA Aviation 2023 Forum*, under review.
- [9] Sutherland, W., "The viscosity of gases and molecular force," *The London, Edinburgh, and Dublin Philosophical Magazine and Journal of Science*, Vol. 36, No. 223, 1893, pp. 507–531.
- [10] Menter, F., "Two-equation eddy-viscosity turbulence models for engineering applications," *AIAA Journal*, Vol. 32, No. 8, 1994, pp. 1598–1605.
- [11] Swarthout, A., MacManus, D., Tejero, F., Matesanz Garcia, J., Boscagli, L., and Sheaf, C., "A comparative assessment of multi-objective optimisation methodologies for aero-engine nacelles," *33rd Congress of the International Council of the Aeronautical Sciences*, 2022.
- [12] Tejero, F., MacManus, D., Matesanz Garcia, J., Swarthout, A., and Sheaf, C., "Towards the design and optimisation of future compact aero-engines: intake/fan-cowl trade-off investigation," *56th 3AF International Conference on Applied Aerodynamics*, FP04–2022.
- [13] Christie, R., Heidebrecht, A., and MacManus, D., "An automated approach to nacelle parameterization using intuitive class shape transformation curves," *Journal of Engineering for Gas Turbines and Power*, Vol. 139, No. 6, 2017.
- [14] Christie, R., Robinson, M., Tejero, F., and MacManus, D., "The use of hybrid intuitive class shape transformation curves in aerodynamic design," *Aerospace Science and Technology*, Vol. 95, 2019, p. 105473.
- [15] Tejero, F., MacManus, D., and Sheaf, C., "Surrogate-based aerodynamic optimisation of compact nacelle aero-engines," *Aerospace Science and Technology*, Vol. 93, 2019, p. 105207.
- [16] Tejero, F., Robinson, M., MacManus, D., and Sheaf, C., "Multi-objective optimisation of short nacelles for high bypass ratio engines," *Aerospace Science and Technology*, Vol. 91, 2019, pp. 410–421.
- [17] Tejero, F., Christie, R., MacManus, D., and Sheaf, C., "Non-axisymmetric aero-engine nacelle design by surrogate-based methods," *Aerospace Science and Technology*, 2021, p. 106890.

- [18] ISO/TC 20/SC 6, "Standard atmosphere," Tech. Rep. International Standard 2533-1975, International Organization for Standardization, 1975.
- [19] Celik, I., Ghia, U., Roache, P., and Freitas, C., "Procedure for estimation and reporting of uncertainty due to discretization in CFD applications," *Journal of Fluids Engineering - Transactions of the ASME*, Vol. 130, No. 7, 2008.
- [20] Deneys Schreiner, B., Tejero, F., MacManus, D., and Sheaf, C., "Robust aerodynamic design of nacelles for future civil aero-engines," *Turbo Expo: Power for Land, Sea, and Air*, Vol. 84058, American Society of Mechanical Engineers, 2020, p. V001T01A015.
- [21] Robinson, M., MacManus, D., Richards, K., and Sheaf, C., "Short and slim nacelle design for ultra-high BPR engines," *55th AIAA Aerospace Sciences Meeting*, 2017–0707.
- [22] Colliss, S., Babinsky, H., Nübler, K., and Lutz, T., "Vortical structures on three-dimensional shock control bumps," *AIAA Journal*, Vol. 54, No. 8, 2016, pp. 2338–2350.
- [23] Gregory, J., Asai, K., Kameda, M., Liu, T., and Sullivan, J., "A review of pressure-sensitive paint for high-speed and unsteady aerodynamics. Proceedings of the Institution of Mechanical Engineers," *Part G: Journal of Aerospace Engineering*, Vol. 222, No. 2, 2008, pp. 249–290.
- [24] Sajben, M., "Uncertainty estimates for pressure sensitive paint measurements," *AIAA Journal*, Vol. 31, No. 11, 1993, pp. 2105–2110.
- [25] Squire, L., "The motion of a thin oil sheet under the steady boundary layer on a body," *Journal of Fluid Mechanics*, Vol. 11, No. 2, 1961, pp. 161–179.
- [26] Sun, C., and Childs, M., "A modified wall wake velocity profile for turbulent compressible boundary layers," *Journal of Aircraft*, Vol. 10, No. 6, 1973, pp. 381–383.
- [27] Musker, A., "Explicit expression for the smooth wall velocity distribution in a turbulent boundary layer," *AIAA Journal*, Vol. 17, No. 6, 1979, pp. 655–657.
- [28] Titchener, N., Colliss, S., and Babinsky, H., "On the calculation of boundary-layer parameters from discrete data," *Experiments in Fluids*, Vol. 56, No. 8, 2015, p. 159.

2023-01-19

A wind tunnel rig to study the external fan cowl separation experienced by compact nacelles in windmilling scenarios

by Sabnis, Kshitiz

AIAA

Sabnis K, Babinsky H, Boscagli L, et al., (2023) A wind tunnel rig to study the external fan cowl separation experienced by compact nacelles in windmilling scenarios. In: AIAA SciTech Forum 2023, 23-27 January 2023, National Harbor, Maryland, USA

<https://doi.org/10.2514/6.2023-1942>

Downloaded from Cranfield Library Services E-Repository